Available online at www.sciencedirect.com
ScienceDirect
Comput. Methods Appl. Mech. Engrg. 371 (2020) 113310
Computer methods in applied mechanics and engineering
www.elsevier.com/locate/cma

Efficient and accurate numerical scheme for a magnetic-coupled phase-field-crystal model for ferromagnetic solid materials

Jun Zhang[a,b], Xiaofeng Yang[c,*]

[a] School of Mathematics and Statistics, Guizhou Key Laboratory of Big Data Statistics Analysis, Guizhou University of Finance and Economics, Guiyang, Guizhou 550025, China
[b] Computational Mathematics Research Center, Guizhou University of Finance and Economics, Guiyang, Guizhou 550025, China
[c] Department of Mathematics, University of South Carolina, Columbia, SC 29208, USA

Received 25 January 2020; received in revised form 25 May 2020; accepted 21 July 2020
Available online 6 August 2020

Abstract

In this paper, we consider numerical approximations for the magnetic-coupled phase-field-crystal model for ferromagnetic solid materials. The governing PDE system consists of two coupled and highly nonlinear equations in which one is the Cahn–Hilliard equation for the density of atoms, and the other is the Allen–Cahn equation for the magnetization field. To solve it, we construct an unconditionally energy stable scheme with the second-order accuracy in time based on the recently developed stabilized-SAV approach. The energy stability of the scheme is proved, and the stability and accuracy are then demonstrated numerically by implementing various numerical examples in 2D and 3D, including the crystal growth and phase separations for both of the magnetic-free and magnetic-coupled cases.

Keywords: Ferromagnetic; Phase-field-crystal; Stabilized-SAV; Allen–Cahn; Cahn–Hilliard; Unconditional energy stability

1. Introduction

Ferromagnetic solid materials, that exhibit a long-range ordering phenomenon at the atomic level, had been greatly used in magnetic-based memory devices such as magnetic tapes, magnetic hard drives, and magnetic random access memory, etc. Since the electromagnetic properties of a solid material including the magnetization and polarization are strongly coupled with the crystalline structure, it is promising to study the polycrystalline microstructure formations in ferromagnetic solids at atomic length scales through mathematical modeling and numerical simulations. In the pioneering work of Elder et. al., in [1–8], a successful approach, called as phase-field-crystal method (PFC, for short), had been developed to simulate the dynamics of the atomic-scale crystal growth. In comparisons with the traditional atomistic simulations (such as molecular dynamics), the PFC model can easily address interfaces and dislocations on the atomic scale since features such as elasticity, dislocations, anisotropy, grain boundaries, and polycrystalline structures naturally emerge in the total free energy functional of it, cf. [2,3,9].

* Corresponding author.
E-mail addresses: jzhang@mail.gufe.edu.cn (J. Zhang), xfyang@math.sc.edu (X. Yang).

https://doi.org/10.1016/j.cma.2020.113310

In this paper, we study numerical approximations for the magnetic-coupled model PFC (FMPFC, for short) for ferromagnetic solid materials that had been developed in [10,11]. By coupling the free energy of the PFC model with the classical Ginzburg–Landau formalism for ferromagnetic ordering, the FMPFC model expands the PFC approach to generate a dissipative model for the ferromagnetic solid below a density-dependent Curie temperature. Formally, the FMPFC system consists of two highly coupled nonlinear equations, where one is the Cahn–Hilliard equation (conserved dynamics) for the density field of atoms (or called as a phase-field variable), and the other is the Allen–Cahn equation (non-conserved dynamics) for the magnetization field. This model appears to be a minimal model with the least number of nonlinear coupling terms between the atoms density field and the magnetization field included in the total free energy. For instance, to incorporate the anisotropy (the dependence of magnetic properties on the crystallographic directions), more degrees of coupling of the magnetization to the gradient of the density were required which in turn brings up a far more complicated system that consists of one extra Cahn–Hilliard equation for concentration field and one extra Allen–Cahn equation for the polarization field, see [12].

However, for algorithm designs, this FMPFC model presents numerous numerical challenges that include a stiffness issue introduced by two nonlinear fourth-order double-well type potentials, as well as the highly coupling nature between the phase-field variable and the magnetization field. It has been well-known that, for the scheme development of gradient flow type models, the main requirement is to develop a scheme that preserves the energy dissipation law unconditionally. This type of scheme is especially preferred for models with high stiffness issues since schemes without following the energy dissipation laws may lead to unstable computations or spurious solutions in practice. Meanwhile, linear and/or decoupled types of schemes are more desirable for the highly coupled nonlinear model from the perspective of practical implementations. We recall that, for the classical PFC model without the magnetic field, enormous successful attempts had been done to obtain energy stable schemes with easy-to-implement properties, for example, the nonlinear convex splitting schemes [13–15], the linear stabilized-explicit scheme [15], the nonlinear quadrature scheme [16], the linear Invariant Energy Quadratization (IEQ) scheme [17], and the linear Scalar Auxiliary Variable (SAV) scheme [15], etc. However, for the highly nonlinear and coupled FMPFC model, as far as the authors know, all accomplishments had been focused on numerical simulations instead of scheme developments, see [10–12].

Therefore, in this paper, we aim to construct an efficient and accurate numerical scheme for solving the FMPFC model. We adopt the SAV approach that is recently developed in [18–23] and modify it to be the stabilized version by introducing some critical stabilization terms to enhance the stability. These stabilization terms are shown to be important to allow large time steps in practice (see Figs. 4.1 and 4.2 in Section 4). The implementation procedure is very simple. First, a nonlocal type auxiliary variable is defined as the square root of the nonlinear part of the free energy and the PDE model is then reformulated in terms of it. By introducing an inverse linear operator, the nonlocal term then vanishes and a linear and decoupled system is finally obtained. At each time step, one only needs to solve several decoupled linear equations, thus the scheme is highly efficient. We prove the unconditional energy stability of the scheme rigorously and further perform various benchmark numerical simulations including the crystal growth and phase separation in two and three-dimensional spaces to demonstrate the accuracy and stability of the scheme, numerically. To the best of the authors' knowledge, the scheme developed in this paper is the first unconditionally energy stable scheme for solving the FMPFC model.

The rest of the article is organized as follows. In Section 2, the governing PDE system for the FMPFC model is presented and the associated energy dissipation law is established. In Section 3, a second-order accurate, linear, and decoupled scheme is developed and its solvability and energy stability are further proved. In Section 4, we perform accuracy and stability tests to show the second-order accuracy and energy stability and present numerous benchmark simulations to show the dynamical morphology of pattern formations of microstructures in two and three-dimensional spaces. Some conclusive remarks are finally given in Section 5.

2. Model and its energy law

We fix some notations here. For each $k \geq 0$, let $(\cdot,\cdot)_k$ and $\|\cdot\|_k$ be the $H^k(\Omega)$ inner product and norm, respectively ($H^0(\Omega) = L^2(\Omega)$). We use $(\cdot,\cdot)$ and $\|\cdot\|$ to denote the L^2 inner product and its norm, respectively. In this paper, all of the bold-lettered symbols represent vectors.

We now introduce the FMPFC model for ferromagnetic solids that were developed in [10,11]. A phase-field variable $\phi(\boldsymbol{x}, t)$ with $\boldsymbol{x} \in \Omega^d$, $d = 2, 3$ and time t, is introduced to describe the particle number density difference

at the point $\boldsymbol{x}$ between the number density of solid atoms and the reference density of liquids at the status of co-existence, $\mathbf{M}(\boldsymbol{x}, t)$ denotes the magnetization field, and $\mathbf{H}(\boldsymbol{x}, t)$ represents the applied external magnetic field.

Hence, the total free energy is a combination of the one-mode PFC formalism for the crystal growth [1–8] and the classical Ginzburg–Landau formalism for ferromagnetic ordering [24] which is described as

$$E(\phi, \mathbf{M}) = E_{PFC}(\phi) + E_{GL}(\mathbf{M}) + E_C(\phi, \mathbf{M}) + E_{ex}(\phi, \mathbf{M}). \tag{2.1}$$

We give a brief introduction for the four parts of the free energy as follows.

- $E_{PFC}(\phi)$ is the free energy for one-mode PFC model that is defined as

$$E_{PFC}(\phi) = \int_\Omega \Big(\frac{\phi}{2} L^2 \phi - \frac{\epsilon}{2}\phi^2 + \frac{1}{4}\phi^4\Big) d\boldsymbol{x}, \tag{2.2}$$

  where $L = \Delta + q_0$, Δ is the Laplace operator, q_0 represents the equilibrium distance between atoms, and ϵ is a positive constant that relates to the temperature of the system.
- $E_{GL}(\mathbf{M})$ is the Ginzburg–Landau free energy for magnetization field that is defined as

$$E_{GL}(\mathbf{M}) = \int_\Omega \left(\frac{w_0}{2}|\nabla \mathbf{M}|^2 - \frac{\alpha}{2}|\mathbf{M}|^2 + \frac{\beta}{4}|\mathbf{M}|^4 - \mathbf{M}\cdot\mathbf{H}\right) d\boldsymbol{x}, \tag{2.3}$$

  where $w_0 > 0$ relates to the exchange correlation length, α and β are two positive phenomenological constants that control the bulk behavior of magnetization, and $\mathbf{H}$ is the external applied magnetic field.
- $E_C(\phi, \mathbf{M})$ is the coupling energy that is defined as

$$E_C(\mathbf{M}) = \int_\Omega \Big(-\gamma \mathbf{M}^2 \phi - \frac{\eta}{2}(\mathbf{M}\cdot\nabla\phi)^2\Big) d\boldsymbol{x}, \tag{2.4}$$

  where the first term induces magnetic islands at atomic sites, the second term gives rise to magneto-elastic coupling, and hence the magnetostriction effect (see [2,10–12] for further discussion of how these parameters relate to material properties).
- $E_{ex}(\phi, \mathbf{M})$ is the extra energy term that is defined as

$$E_{ex}(\phi, \mathbf{M}) = \int_\Omega \left(\frac{\theta_1}{6}|\mathbf{M}|^6 + \frac{\theta_2}{4}|\nabla\phi|^4\right) d\boldsymbol{x}, \tag{2.5}$$

  where $0 < \theta_1, \theta_2 \ll 1$. These two terms are simply introduced to make the total energy bounded from below.

Remark 2.1. Remarkably, the total free energy given in the references [10–12] only includes E_{PFC}, E_{GL}, and E_C. However, it is highly non-trivial to prove such a free energy to be bounded from below where the main challenge lies in how to bound the second coupling terms in E_C. To this end, instead of controlling the magnitude of model parameters or the complex Sobolev embedding inequality for the terms of $\nabla\phi$ and $\Delta\phi$, we introduce two extra higher order terms in E_{ex}. In this way, it becomes very straight forward to show that the total energy is bounded from below as long as the two parameters θ_1 and θ_2 are nonzero. The details are shown in Lemma 3.1.

By using the Cahn–Hilliard dynamics, i.e., the H^{-1}-gradient flow approach for the atoms density phase-field variable ϕ, and the Allen–Cahn dynamics, i.e., the L^2-gradient flow approach for the magnetization field, the state of the system that relates the temporal changes of the two variables $\phi(\boldsymbol{x}, t)$ and $\mathbf{M}(\boldsymbol{x}, t)$ is governed by the following equations:

$$\begin{cases} \phi_t = M_1 \Delta \mu_1, \\ \mu_1 = \dfrac{\delta E(\phi, \mathbf{M})}{\delta \phi}, \\ -\mathbf{M}_t = M_2 \mu_2, \\ \mu_2 = \dfrac{\delta E(\phi, \mathbf{M})}{\delta \mathbf{M}}, \end{cases} \tag{2.6}$$

where $M_1, M_2 > 0$ are the mobility constants, μ_1 and μ_2 are two chemical potentials derived by the variational derivative of the total free energy.

By taking the total free energy described in (2.1), the PDE system (2.6) turns into

$$\phi_t = M_1 \Delta \mu_1, \tag{2.7}$$

$$\mu_1 = L^2\phi + \phi^3 - \epsilon\phi + \eta\nabla\cdot((\mathbf{M}\cdot\nabla\phi)\mathbf{M}) - \gamma\mathbf{M}^2 - \theta_2\nabla\cdot(|\nabla\phi|^2\nabla\phi), \tag{2.8}$$

$$\begin{aligned} -\mathbf{M}_t = M_2(&-w_0\Delta\mathbf{M} - \alpha\mathbf{M} + \beta(\mathbf{M}\cdot\mathbf{M})\mathbf{M} - \mathbf{H} \\ &-2\gamma\mathbf{M}\phi - \eta(\mathbf{M}\cdot\nabla\phi)\nabla\phi + \theta_1|\mathbf{M}|^4\mathbf{M}), \end{aligned} \tag{2.9}$$

where the initial conditions are set as $\phi(t=0) = \phi^0$ and $\mathbf{M}(t=0) = \mathbf{M}^0$.

Concerning the boundary conditions, in this work, we consider the square domain and assume the periodic boundary conditions are satisfied for all variables. Thus all complexities affiliated with the boundary integrals caused by integration by parts can be removed. Alternative boundary conditions can be the no-flux type as

$$\partial_{\mathbf{n}}\phi|_{\partial\Omega} = \partial_{\mathbf{n}}\mu_1|_{\partial\Omega} = \partial_{\mathbf{n}}\mathbf{M}|_{\partial\Omega} = 0, \tag{2.10}$$

where $\mathbf{n}$ is the outward normal on the boundary. All numerical analyses in this paper are applicable to the no-flux boundary conditions without any further difficulties.

It is easy to see that the model (2.7)–(2.9) follows the energy dissipation law. We take the L^2 inner product of (2.7) with $-\mu_1$, and of (2.8) with ϕ_t, of (2.9) with $-\frac{1}{M_2}\mathbf{M}_t$, perform integration by parts, and take the summation of all equalities to obtain

$$\frac{d}{dt}E(\phi,\mathbf{M}) \le -M_1\|\nabla\mu_1\|^2 - \frac{1}{M_2}\|\mathbf{M}_t\|^2 - (\mathbf{H},\mathbf{M}_t). \tag{2.11}$$

By using the Cauchy–Schwarz inequality, we derive

$$-(\mathbf{H},\mathbf{M}_t) \le \frac{1}{2M_2}\|\mathbf{M}_t\|^2 + \frac{M_2}{2}\|\mathbf{H}\|^2. \tag{2.12}$$

Hence, the energy law becomes

$$\frac{d}{dt}E(\phi,\mathbf{M}) \le -M_1\|\nabla\mu_1\|^2 - \frac{1}{2M_2}\|\mathbf{M}_t\|^2 + \frac{M_2}{2}\|\mathbf{H}\|^2. \tag{2.13}$$

Remark 2.2. The FMPFC system (2.7)–(2.9) degenerates to the classical PFC model (magnetic-free case) if we set $\beta = \gamma = \theta_2 = 0$ in (2.8), that reads as

$$\phi_t = M_1\Delta\mu_1, \tag{2.14}$$

$$\mu_1 = L^2\phi + \phi^3 - \epsilon\phi. \tag{2.15}$$

We note that the main numerical issue to develop energy stable scheme for the PFC system (2.14)–(2.15) lies on the temporal discretization of the only nonlinear term ϕ^3. Compared with it, it is obvious the FMPFC model (2.7)–(2.9) include many coupled nonlinear terms and thus it presents much more numerical challenges to obtain schemes with unconditional energy stability.

3. Numerical schemes

In this section, for the highly coupled nonlinear system (2.7)–(2.9), we construct a numerical scheme which is linear, decoupled, and second-order accurate in time. We mainly adopt the recently developed SAV approach [18–23] but modify it by introducing several linear stabilization terms to improve energy stability. Numerical results show that these stabilization terms are effective for stability improvement, particularly when large time steps are used. The details are shown as follows.

We first establish a bounded-from-below property for the nonlinear part of the total free energy (2.1) as follows.

Lemma 3.1. *For any positive constants θ_1 and θ_2, there always exists a constant C such that*

$$G(\phi,\mathbf{M}) \ge C, \tag{3.1}$$

where $G(\phi,\mathbf{M})$ includes all nonlinear terms in $E(\phi,\mathbf{M})$ that is defined as

$$G(\phi,\mathbf{M}) = \int_\Omega \Big(\frac{1}{4}\phi^4 - \frac{\epsilon}{2}\phi^2 - \frac{\alpha}{2}|\mathbf{M}|^2 + \frac{\beta}{4}|\mathbf{M}|^4 - \gamma\mathbf{M}^2\phi - \frac{\eta}{2}(\mathbf{M}\cdot\nabla\phi)^2 + \frac{\theta_1}{6}|\mathbf{M}|^6 + \frac{\theta_2}{4}|\nabla\phi|^4\Big)d\boldsymbol{x}.$$

Proof. We only need to show the two coupling terms can be bounded by other terms. From Young's inequality, it is easy to derive

$$-\gamma \mathbf{M}^2\phi \geq -|\gamma|(\frac{1}{2}|\mathbf{M}|^4 + \frac{1}{2}\phi^2), \tag{3.2}$$

and

$$-\frac{\eta}{2}(\mathbf{M}\cdot\nabla\phi)^2 \geq -\frac{\theta_2}{8}|\nabla\phi|^4 - \frac{\eta^2}{2\theta_2}|\mathbf{M}|^4. \tag{3.3}$$

Therefore, we obtain

$$G(\phi,\mathbf{M}) \geq \int_\Omega \left(\frac{\theta_2}{8}|\nabla\phi|^4 + \frac{1}{4}\phi^4 + a\phi^2 + \frac{\theta_1}{6}|\mathbf{M}|^6 + b|\mathbf{M}|^4 + c|\mathbf{M}|^2\right) d\boldsymbol{x}. \tag{3.4}$$

where a, b, c (may not be positive) are the constants after combining the terms of same kind. It is easy to see that, for any a, b, c, there always exists a constant C such that (3.1) is valid as long as the two given constants θ_1 and θ_2 are positive. □

We split the total free energy (2.1) into the linear part and the nonlinear part, as follows.

$$E(\phi,\mathbf{M}) = \int_\Omega \left(\frac{\phi}{2}L^2\phi + \frac{w_0}{2}|\nabla\mathbf{M}|^2\right) d\boldsymbol{x} + G(\phi,\mathbf{M}), \tag{3.5}$$

and define an auxiliary non-local function $u(t)$ to quadratize $G(\phi,\mathbf{M})$, i.e.,

$$u(t) = \sqrt{G(\phi,\mathbf{M}) + B}, \tag{3.6}$$

where B is a constant such the radicand $G(\phi,\mathbf{M})+B > 0$. By using the new variable u, we recast the pseudo-energy functional (2.1) as

$$E(\phi,\mathbf{M},u) = \int_\Omega \left(\frac{\phi}{2}L^2\phi + \frac{w_0}{2}|\nabla\mathbf{M}|^2\right) d\boldsymbol{x} + u^2 - B. \tag{3.7}$$

By taking the time derivative for the new variable $u(t)$, we can rewrite the system (2.7)–(2.9) to be the following system,

$$\phi_t = M_1\Delta\mu_1, \tag{3.8}$$

$$\mu_1 = L^2\phi + uR, \tag{3.9}$$

$$-\frac{1}{M_2}\mathbf{M}_t = -w_0\Delta\mathbf{M} + \mathbf{R}u - \mathbf{H}, \tag{3.10}$$

$$u_t = \frac{1}{2}\int_\Omega (R\phi_t + \mathbf{R}\cdot\mathbf{M}_t)d\boldsymbol{x}, \tag{3.11}$$

where

$$\begin{cases} R(\phi,\mathbf{M}) = \dfrac{\phi^3 - \epsilon\phi + \eta\nabla\cdot((\mathbf{M}\cdot\nabla\phi)\mathbf{M}) - \gamma\mathbf{M}^2 - \theta_2\nabla\cdot(|\nabla\phi|^2\nabla\phi)}{\sqrt{G(\phi,\mathbf{M})+B}}, \\ \mathbf{R}(\phi,\mathbf{M}) = \dfrac{-\alpha\mathbf{M} + \beta(\mathbf{M}\cdot\mathbf{M})\mathbf{M} - 2\gamma\mathbf{M}\phi - \eta(\mathbf{M}\cdot\nabla\phi)\nabla\phi + \theta_1|\mathbf{M}|^4\mathbf{M}}{\sqrt{G(\phi,\mathbf{M})+B}}. \end{cases} \tag{3.12}$$

The initial conditions of the above system are given as

$$\phi(t=0) = \phi^0, \mathbf{M}(t=0) = \mathbf{M}^0, u(t=0) = \sqrt{G(\phi^0,\mathbf{M}^0)+B}. \tag{3.13}$$

Note the transformed system (3.8)–(3.11) is equivalent to the original system (2.7)–(2.9). Hence these two systems share the same boundary conditions. Meanwhile, the system (3.8)–(3.11) also preserves the energy dissipative law which is derived as follows. After taking the L^2 inner product of (3.8) with $-\mu_1$, of (3.9) with ϕ_t, of (3.10) with $\mathbf{M}_t$, and multiplying (3.11) with $2u$, performing integration by parts, and summing all equalities up, we can obtain the energy dissipation law as

$$\frac{d}{dt}E(\phi,\mathbf{M},u) = -M_1\|\nabla\mu_1\|^2 - \frac{1}{M_2}\|\mathbf{M}_t\|^2 \leq 0. \tag{3.14}$$

For a given positive integer N, we set $t^n = n\delta t, 0 \le n \le N$, where $\delta t = T/N$ be the time step size and let ψ^n be the numerical approximation to the analytic function $\psi(\cdot, t)|_{t=t^n}$.

By using the second-order backward differentiation formula (BDF2) for the time derivative, and simple implicit–explicit combinations for the nonlinear terms, we construct a numerical scheme for solving the system (3.8)–(3.11) that reads as follows.

We update ϕ^{n+1}, $\mathbf{M}^{n+1}$, and u^{n+1} by solving the following scheme

$$\frac{3\phi^{n+1} - 4\phi^n + \phi^{n-1}}{2\delta t} = M_1 \Delta \mu_1^{n+1}, \tag{3.15}$$

$$\mu_1^{n+1} = L^2\phi^{n+1} + u^{n+1}R^{*,n+1} + S_1(\phi^{n+1} - \phi^{*,n+1}) - S_2\Delta(\phi^{n+1} - \phi^{*,n+1}), \tag{3.16}$$

$$-\frac{3\mathbf{M}^{n+1} - 4\mathbf{M}^n + \mathbf{M}^{n-1}}{2M_2\delta t} = -w_0\Delta\mathbf{M}^{n+1} - \mathbf{H} + u^{n+1}\mathbf{R}^{*,n+1} + S_3(\mathbf{M}^{n+1} - \mathbf{M}^{*,n+1}), \tag{3.17}$$

$$\begin{aligned} 3u^{n+1} - 4u^n + u^{n-1} = \frac{1}{2}\int_\Omega \Big(& R^{*,n+1}(3\phi^{n+1} - 4\phi^n + \phi^{n-1}) \\ & + \mathbf{R}^{*,n+1}\cdot(3\mathbf{M}^{n+1} - 4\mathbf{M}^n + \mathbf{M}^{n-1}) \Big)\, d\boldsymbol{x}, \end{aligned} \tag{3.18}$$

where $(\phi, \mathbf{M}, u)^n$ and $(\phi, \mathbf{M}, u)^{n-1}$ are assumed to be known,

$$\begin{aligned} &\phi^{*,n+1} = 2\phi^n - \phi^{n-1},\ \mathbf{M}^{*,n+1} = 2\mathbf{M}^n - \mathbf{M}^{n-1}, \\ &R^{*,n+1} = R(\phi^{*,n+1}, \mathbf{M}^{*,n+1}),\ \mathbf{R}^{*,n+1} = \mathbf{R}(\phi^{*,n+1}, \mathbf{M}^{*,n+1}), \end{aligned} \tag{3.19}$$

and S_1, S_2, S_3 are three positive stabilization parameters. Note $\mathbf{H}$ is the constant applied external field treated as a forcing term.

In the above-developed scheme, we add three linear stabilization terms in (3.16) and (3.17) to improve stability. This is because the nonlinear terms are treated explicitly in H and $\mathbf{R}$. Although these stabilization terms bring up extra splitting errors, the orders of errors are comparable to that induced by the linear extrapolation of the nonlinear terms. Therefore, in practice, when the three stabilization constants are set as $S_1 \sim O(1)$ (to balance the cubic term ϕ^3), $S_2 \sim O(\eta)$ (to balance the term $(\eta\nabla\cdot((\mathbf{M}\cdot\nabla\phi)\nabla\phi))$), and $S_3 \sim max(\beta, \gamma, \eta)$ (to balance $\beta(\mathbf{M}\cdot\mathbf{M})\mathbf{M}$, $\gamma\mathbf{M}\phi$, and $(\eta(\mathbf{M}\cdot\nabla\phi)\nabla\phi)$), numerical evidences show that the scheme achieves the best balance between the stability and accuracy. While adopting large time steps, these stabilization terms are critical to enhance the stability which is demonstrated by numerous numerical examples, cf. Figs. 4.1 and 4.2, where we give the detailed comparisons in the accuracy and stability computed by the developed scheme with and without the stabilization terms.

Even though the scheme (3.15)–(3.18) provides a linear system, the three unknowns ϕ^{n+1}, $\mathbf{M}^{n+1}$, and u^{n+1} are nonlinearly coupled together thus some costly iterative solvers are needed. Hence, to overcome this difficulty in practice, we implement the scheme by the following decoupling process which also eliminates the computations of the nonlocal term of u^{n+1} in the meantime. Details are shown below.

We rewrite (3.18) as follows,

$$u^{n+1} = \frac{1}{2}\int_\Omega R^{*,n+1}\phi^{n+1}d\boldsymbol{x} + \frac{1}{2}\int_\Omega \mathbf{R}^{*,n+1}\cdot\mathbf{M}^{n+1}d\boldsymbol{x} + g^n, \tag{3.20}$$

where g^n includes all explicit terms that read as

$$g^n = \frac{4u^n - u^{n-1}}{3} - \frac{1}{2}\int_\Omega R^{*,n+1}\frac{4\phi^n - \phi^{n-1}}{3}d\boldsymbol{x} - \frac{1}{2}\int_\Omega \mathbf{R}^{*,n+1}\cdot\frac{4\mathbf{M}^n - \mathbf{M}^{n-1}}{3}d\boldsymbol{x}.$$

Then the scheme (3.15)–(3.18) can be combined together to be the following two coupled nonlocal type equations

$$\mathscr{D}(\phi^{n+1}) - \frac{1}{2}\Delta R^{*,n+1}\left(\int_\Omega R^{*,n+1}\phi^{n+1}d\boldsymbol{x} + \int_\Omega \mathbf{R}^{*,n+1}\cdot\mathbf{M}^{n+1}d\boldsymbol{x}\right) = \tilde{g}_1^n, \tag{3.21}$$

$$\mathbf{D}(\mathbf{M}^{n+1}) + \frac{1}{2}\mathbf{R}^{*,n+1}\left(\int_\Omega R^{*,n+1}\phi^{n+1}d\boldsymbol{x} + \int_\Omega \mathbf{R}^{*,n+1}\cdot\mathbf{M}^{n+1}d\boldsymbol{x}\right) = \tilde{\mathbf{g}}_2^n, \tag{3.22}$$

where the operators $\mathscr{D}$ and $\mathbf{D}$ are defined as

$$\begin{aligned}\mathscr{D}(\psi) &= \frac{3}{2M_1\delta t}\psi - \Delta L^2\psi - S_1\Delta\psi + S_2\Delta^2\psi,\\ \mathbf{D}(\mathbf{M}) &= \frac{3}{2M_2\delta t}\mathbf{M} - w_0\Delta\mathbf{M} + S_3\mathbf{M},\end{aligned} \tag{3.23}$$

for any arbitrary functions ψ and $\mathbf{M}$, and the two terms on the right hand side $\tilde{g}_1^n$ and $\tilde{\mathbf{g}}_2^n$ include all explicit terms.

We define a linear inverse operator $\mathscr{D}^{-1}(\cdot)$ and $\mathbf{D}^{-1}(\cdot)$, such that for any periodic functions $\phi, \mathbf{M} \in L^2(\Omega)$, $\psi = \mathscr{D}^{-1}(\phi)$ and $\mathbf{Q} = \mathbf{D}^{-1}(\mathbf{M})$ are the solutions of the two linear systems as

$$\mathscr{D}(\psi) = \phi, \quad \mathbf{D}(\mathbf{Q}) = \mathbf{M}, \tag{3.24}$$

with the periodic boundary conditions.

By applying the operator $\mathscr{D}^{-1}$ to (3.21) and $\mathbf{D}^{-1}$ to (3.22), we obtain

$$\phi^{n+1} - \frac{1}{2}\mathscr{D}^{-1}(\Delta R^{*,n+1})\left(\int_\Omega R^{*,n+1}\phi^{n+1}d\boldsymbol{x} + \int_\Omega \mathbf{R}^{*,n+1}\cdot\mathbf{M}^{n+1}d\boldsymbol{x}\right) = \mathscr{D}^{-1}(\tilde{g}_1^n), \tag{3.25}$$

$$\mathbf{M}^{n+1} + \frac{1}{2}\mathbf{D}^{-1}(\mathbf{R}^{*,n+1})\left(\int_\Omega R^{*,n+1}\phi^{n+1}d\boldsymbol{x} + \int_\Omega \mathbf{R}^{*,n+1}\cdot\mathbf{M}^{n+1}d\boldsymbol{x}\right) = \mathbf{D}^{-1}(\tilde{\mathbf{g}}_2^n). \tag{3.26}$$

We take the L^2 inner product of (3.25) with $R^{*,n+1}$, and of (3.26) with $\mathbf{R}^{*,n+1}$ to obtain the following 2×2 matrix system

$$\begin{bmatrix} 1+a & a \\ b & 1+b \end{bmatrix}\begin{bmatrix} \int_\Omega R^{*,n+1}\phi^{n+1}d\boldsymbol{x} \\ \int_\Omega \mathbf{R}^{*,n+1}\cdot\mathbf{M}^{n+1}d\boldsymbol{x} \end{bmatrix} = \begin{bmatrix} \int_\Omega R^{*,n+1}\mathscr{D}^{-1}(\tilde{g}_1^n)d\boldsymbol{x} \\ \int_\Omega \mathbf{R}^{*,n+1}\cdot\mathbf{D}^{-1}(\tilde{\mathbf{g}}_2^n)d\boldsymbol{x} \end{bmatrix}, \tag{3.27}$$

where

$$a = -\frac{1}{2}\int_\Omega R^{*,n+1}\mathscr{D}^{-1}(\Delta R^{*,n+1})d\boldsymbol{x},\ b = \frac{1}{2}\int_\Omega \mathbf{R}^{*,n+1}\cdot\mathbf{D}^{-1}(\mathbf{R}^{*,n+1})d\boldsymbol{x}. \tag{3.28}$$

We need to verify that determinant of the 2×2 matrix on the left-hand side is nonzero. A simple calculation gives

$$\begin{aligned} det &= 1 + a + b\\ &= 1 - \frac{1}{2}\int_\Omega R^{*,n+1}\mathscr{D}^{-1}(\Delta R^{*,n+1})d\boldsymbol{x} + \frac{1}{2}\int_\Omega \mathbf{R}^{*,n+1}\cdot\mathbf{D}^{-1}(\mathbf{R}^{*,n+1})d\boldsymbol{x}.\end{aligned} \tag{3.29}$$

It is easy to check that $-\int_\Omega R^{*,n+1}\mathscr{D}^{-1}(\Delta R^{*,n+1})d\boldsymbol{x} \geq 0$ and $\int_\Omega \mathbf{R}^{*,n+1}\cdot\mathbf{D}^{-1}(\mathbf{R}^{*,n+1})d\boldsymbol{x} \geq 0$ since $-\mathscr{D}^{-1}(\Delta)$ and $\mathbf{D}^{-1}$ are both positive definite. Therefore $det \neq 0$ implies the linear system (3.27) is uniquely solvable.

Furthermore, (3.27) can be regarded as an explicit formulation for the two nonlocal terms $\int_\Omega R^{*,n+1}\phi^{n+1}d\boldsymbol{x}$ and $\int_\Omega \mathbf{R}^{*,n+1}\cdot\mathbf{M}^{n+1}d\boldsymbol{x}$. Therefore, in computations, we first find

$$\begin{aligned}&\psi_1 = \mathscr{D}^{-1}(\tilde{g}_1^n), \quad \psi_2 = \mathscr{D}^{-1}(\Delta R^{*,n+1}),\\ &\mathbf{Q}_1 = \mathbf{D}^{-1}(\tilde{\mathbf{g}}_2^n), \quad \mathbf{Q}_2 = \mathbf{D}^{-1}(\mathbf{R}^{*,n+1}),\end{aligned}$$

that means to solve the following four decoupled linear equations formed as,

$$\begin{aligned}&\left(\frac{3}{2M_1\delta t} - \Delta L^2 - S_1\Delta + S_2\Delta^2\right)\psi_i = \tilde{g}_1^n,\ \Delta R^{*,n+1},\ i = 1,2,\\ &\left(\frac{3}{2M_2\delta t} - w_0\Delta + S_3\right)\mathbf{Q}_i = \tilde{\mathbf{g}}_2^n,\ \mathbf{R}^{*,n+1},\ i = 1,2,\end{aligned} \tag{3.30}$$

with the periodic boundary conditions. And then, after by applying (3.27) to obtain $\int_\Omega R^{*,n+1}\phi^{n+1}d\boldsymbol{x}$ and $\int_\Omega \mathbf{R}^{*,n+1}\cdot\mathbf{M}^{n+1}d\boldsymbol{x}$, we can obtain ϕ^{n+1} and $\mathbf{M}^{n+1}$ from (3.25) and (3.26) directly.

Hence, from the decoupling process presented above, we find that the total cost at each time step is just *solving four decoupled linear equations with constant coefficients*. Since the system is equipped with periodic boundary conditions, these equations can be easily solved when using the Fourier-Spectral method. Thus this scheme is highly efficient and easy to implement.

The unconditionally energy stability of the numerical scheme (3.15)–(3.18) is shown as follows.

Theorem 3.1. *The scheme (3.15)–(3.18) follows a discrete energy dissipation law as*

$$\frac{1}{\delta t}(E^{n+1}-E^n)\leq -M_1\|\nabla\mu_1^{n+1}\|^2-\frac{1}{2M_2}\left\|\frac{3\mathbf{M}^{n+1}-4\mathbf{M}^n+\mathbf{M}^{n-1}}{2\delta t}\right\|^2+\frac{M_2}{2}\|\mathbf{H}\|^2, \tag{3.31}$$

where

$$\begin{aligned}E^{n+1}=&\frac{1}{2}\left(\frac{\|L\phi^{n+1}\|^2+\|L(2\phi^{n+1}-\phi^n)\|^2}{2}\right)+\frac{w_0}{2}\left(\frac{\|\nabla\mathbf{M}^{n+1}\|^2+\|\nabla(2\mathbf{M}^{n+1}-\mathbf{M}^n)\|^2}{2}\right)\\&+\frac{(u^{n+1})^2+(2u^{n+1}-u^n)^2}{2}+S_1\frac{\|\phi^{n+1}-\phi^n\|^2}{2}+S_2\frac{\|\nabla\phi^{n+1}-\nabla\phi^n\|^2}{2}+S_3\frac{\|\mathbf{M}^{n+1}-\mathbf{M}^n\|^2}{2}.\end{aligned}$$

Proof. First, by taking the L^2 inner product of (3.15) with $-2\delta t\mu_1^{n+1}$, we obtain

$$-(3\phi^{n+1}-4\phi^n+\phi^{n-1},\mu_1^{n+1})=2\delta tM_1\|\nabla\mu_1^{n+1}\|^2. \tag{3.32}$$

Second, by taking the L^2 inner product of (3.16) with $3\phi^{n+1}-4\phi^n+\phi^{n-1}$, and using integration by parts, we obtain

$$\begin{aligned}(\mu_1^{n+1},3\phi^{n+1}-4\phi^n+\phi^{n-1})=&(L\phi^{n+1},L(3\phi^{n+1}-4\phi^n+\phi^{n-1}))\\&+u^{n+1}(R^{*,n+1},3\phi^{n+1}-4\phi^n+\phi^{n-1})\\&+S_1(\phi^{n+1}-2\phi^n+\phi^{n-1},3\phi^{n+1}-4\phi^n+\phi^{n-1})\\&+S_2(\nabla(\phi^{n+1}-2\phi^n+\phi^{n-1}),\nabla(3\phi^{n+1}-4\phi^n+\phi^{n-1})).\end{aligned} \tag{3.33}$$

Third, by taking the L^2 inner product of (3.17) with $3\mathbf{M}^{n+1}-4\mathbf{M}^n+\mathbf{M}^{n-1}$, and using integration by parts, we obtain

$$\begin{aligned}-\frac{1}{2M_2\delta t}\|3\mathbf{M}^{n+1}-4\mathbf{M}^n+\mathbf{M}^{n-1}\|^2=&w_0(\nabla\mathbf{M}^{n+1},\nabla(3\mathbf{M}^{n+1}-4\mathbf{M}^n+\mathbf{M}^{n-1}))\\&-(\mathbf{H},3\mathbf{M}^{n+1}-4\mathbf{M}^n+\mathbf{M}^{n-1})\\&+u^{n+1}(\mathbf{R}^{*,n+1},3\mathbf{M}^{n+1}-4\mathbf{M}^n+\mathbf{M}^{n-1})\\&+S_3(\mathbf{M}^{n+1}-2\mathbf{M}^n+\mathbf{M}^{n-1},3\mathbf{M}^{n+1}-4\mathbf{M}^n+\mathbf{M}^{n-1}).\end{aligned} \tag{3.34}$$

Fourth, by multiplying (3.18) with $-2u^{n+1}$, we obtain

$$\begin{aligned}-2(3u^{n+1}-4u^n+u^{n-1})u^{n+1}=&-u^{n+1}\int_\Omega R^{*,n+1}(3\phi^{n+1}-4\phi^n+\phi^{n-1})d\boldsymbol{x}\\&-u^{n+1}\int_\Omega\mathbf{R}^{*,n+1}(3\mathbf{M}^{n+1}-4\mathbf{M}^n+\mathbf{M}^{n-1})d\boldsymbol{x}.\end{aligned} \tag{3.35}$$

Finally, we combine the above equations and apply the following two identities

$$\begin{aligned}&2a(3a-4b+c)=a^2+(2a-b)^2-b^2-(2b-c)^2+(a-2b+c)^2,\\&(3a-4b+c)(a-2b+c)=(a-b)^2-(b-c)^2+2(a-2b+c)^2,\end{aligned} \tag{3.36}$$

to arrive at

$$\begin{aligned}
&\frac{1}{2}(\|L\phi^{n+1}\|^2+\|L(2\phi^{n+1}-\phi^n)\|^2)-\frac{1}{2}(\|L\phi^n\|^2+\|L(2\phi^n-\phi^{n-1})\|^2)\\
&+\frac{w_0}{2}(\|\nabla\mathbf{M}^{n+1}\|^2+\|\nabla(2\mathbf{M}^{n+1}-\mathbf{M}^n)\|^2)-\frac{w_0}{2}(\|\nabla\mathbf{M}^n\|^2+\|\nabla(2\mathbf{M}^n-\mathbf{M}^{n-1})\|^2)\\
&+\left((u^{n+1})^2+(2u^{n+1}-u^n)^2\right)-\left((u^n)^2+(2u^n-u^{n-1})^2\right)\\
&+S_1\|\phi^{n+1}-\phi^n\|^2-S_1\|\phi^n-\phi^{n-1}\|^2+S_2\|\nabla\phi^{n+1}-\nabla\phi^n\|^2-S_2\|\nabla\phi^n-\nabla\phi^{n-1}\|^2\\
&+S_3\|\mathbf{M}^{n+1}-\mathbf{M}^n\|^2-S_3\|\mathbf{M}^n-\mathbf{M}^{n-1}\|^2\\
&+\Big\{\frac{1}{2}\|L\phi^{n+1}-2L\phi^n+L\phi^{n-1}\|^2+\frac{w_0}{2}\|\nabla(\mathbf{M}^{n+1}-2\mathbf{M}^n+\mathbf{M}^{n-1})\|^2\\
&+(u^{n+1}-2u^n+u^{n-1})^2+2S_1\|\phi^{n+1}-2\phi^n+\phi^{n-1}\|^2\\
&+2S_2\|\nabla\phi^{n+1}-2\nabla\phi^n+\nabla\phi^{n-1}\|^2+2S_3\|\nabla\mathbf{M}^{n+1}-2\nabla\mathbf{M}^n+\nabla\mathbf{M}^{n-1}\|^2\Big\}\\
&=-2\delta t M_1\|\nabla\mu_1^{n+1}\|^2-2\delta t\frac{1}{M_2}\left\|\frac{3\mathbf{M}^{n+1}-4\mathbf{M}^n+\mathbf{M}^{n-1}}{2\delta t}\right\|^2+(\mathbf{H},3\mathbf{M}^{n+1}-4\mathbf{M}^n+\mathbf{M}^{n-1}).
\end{aligned}$$

For the last term on the right end, by using the Cauchy–Schwarz inequality, we derive

$$(\mathbf{H},3\mathbf{M}^{n+1}-4\mathbf{M}^n+\mathbf{M}^{n-1})\le\delta t\frac{1}{M_2}\left\|\frac{3\mathbf{M}^{n+1}-4\mathbf{M}^n+\mathbf{M}^{n-1}}{2\delta t}\right\|^2+M_2\delta t\|\mathbf{H}\|^2. \tag{3.37}$$

This concludes (3.31) after we drop all positive terms in {}. □

Remark 3.1. Heuristically, $\frac{1}{\delta t}(E^{n+1}-E^n)$ is a second-order approximation of $\frac{d}{dt}E(u,\phi,\mathbf{M})$ at $t=t^{n+1}$. For any smooth variable ψ with time, we have

$$\begin{aligned}
&\frac{\|\psi^{n+1}\|^2-\|2\psi^{n+1}-\psi^n\|^2}{2\delta t}-\frac{\|\psi^n\|^2-\|2\psi^n-\psi^{n-1}\|^2}{2\delta t}\\
&\qquad\cong\frac{\|\psi^{n+2}\|^2-\|\psi^n\|^2}{2\delta t}+O(\delta t^2)\cong\frac{d}{dt}\|\psi(t^{n+1})\|^2+O(\delta t^2),
\end{aligned}\tag{3.38}$$

and

$$\frac{\|\psi^{n+1}-\psi^n\|^2-\|\psi^n-\psi^{n-1}\|^2}{2\delta t}\cong O(\delta t^2). \tag{3.39}$$

Remark 3.2. The computations of second-order time-discrete scheme (3.15)–(3.18) need the values of ϕ^1, $\mathbf{M}^1$ and u^1. In practice, we obtain them by developing a similar first-order time marching scheme where the backward Euler formulation is used for time derivative, that reads as,

$$\begin{aligned}
&\frac{\phi^1-\phi^0}{\delta t}=M_1\Delta\mu_1^1,\\
&\mu_1^1=L^2\phi^1+u^1R^0+S_1(\phi^1-\phi^0)-S_2\Delta(\phi^1-\phi^0),\\
&-\frac{\mathbf{M}^1-\mathbf{M}^0}{M_2\delta t}=-w_0\Delta\mathbf{M}^1-\mathbf{H}+u^1\mathbf{R}^0+S_3(\mathbf{M}^1-\mathbf{M}^0),\\
&u^1-u^0=\frac{1}{2}\int_\Omega\left(R^0(\phi^1-\phi^0)+\mathbf{R}^0\cdot(\mathbf{M}^1-\mathbf{M}^0)\right)d\boldsymbol{x},
\end{aligned}\tag{3.40}$$

where $R^0=R(\phi^0,\mathbf{M}^0)$ and $\mathbf{R}^0=\mathbf{R}(\phi^0,\mathbf{M}^0)$.

Remark 3.3. The theoretical results derived in this paper can be carried over to any consistent finite-dimensional Galerkin approximations in the space even though the only time-discrete scheme is considered here since the proofs are all based on a variational formulation with all test functions in the same space as the space of the trial functions.

4. Numerical examples

In this section, we present numerical experiments to solve the FMPFC model by implementing the developed scheme (3.15)–(3.18). The numerical examples include the accuracy/stability tests in the refinement of time step size, and the benchmark simulations of crystal growth, as well as the phase separation examples. For each simulation, we compare the magnetic-free and magnetic-coupled cases to investigate how the magnetic field motivates the pattern formation.

We use a square 2D or 3D computed domain as $\Omega = [0, L]^d$ with $d = 2, 3$ and adopt Fourier-spectral method for the space discretization since the periodic boundary conditions are assumed for all variables. Meanwhile, we choose sufficient spatial resolutions to guarantee that the spatial gradients are fully resolved.

4.1. Accuracy and stability test

We first perform refinement tests for temporal convergence of the proposed scheme, the stabilized-SAV scheme (3.15)–(3.18), denoted by SSAV for short. To see the effectiveness of the stabilizers, we also compute the convergence rates of the non-stabilized version, namely, the scheme (3.15)–(3.18) but with $S_1 = S_2 = S_3 = 0$, denoted by SAV for short.

We set the 2D computational domain as $\Omega = [0, 128]^2$ and use 129^2 Fourier modes to discretize the space so that the error from spatial discretization is neglected compared with the time discretization. The initial conditions read as

$$\begin{cases} \phi^0 = \sin(\omega x)\cos(\omega y), \\ \mathbf{M}^0 = (\mathbf{M}_1^0, \mathbf{M}_2^0) = (\sin(\omega x)\sin(\omega y), \cos(\omega x)\cos(\omega y)), \\ \mathbf{H} = (\mathbf{H}_1, \mathbf{H}_2) = (\sin(\omega x)\cos(\frac{1}{2}\omega y), \cos(\frac{1}{2}\omega y)), \end{cases} \tag{4.1}$$

with $\omega = \frac{8\pi}{128}$. Since the exact solutions of the system are not known, we treat the numerical solutions obtained with a very tiny time step size $\delta t = 1\mathrm{e}-9$ computed by the scheme SSAV as the exact solution. By varying the time step sizes, we compute the average of the L^2 errors of the phase function ϕ and $\mathbf{M}$ between the exact and approximate solutions at time $t = 10$.

The model parameters are set as follows,

$$M_1 = 1,\ M_2 = 0.01,\ q_0 = 1, \epsilon = 0.05, B = 1\mathrm{e}7, \alpha = 1, \beta = 10, \theta_1 = \theta_2 = 1\mathrm{e}-9. \tag{4.2}$$

We vary the two coupling parameters γ, η to test the convergence rates.

First, we test the low stiffness case by setting relatively small values of $\gamma = 0.01$ and $\eta = -0.1$. In Fig. 4.1(a), we plot the average of L^2 numerical errors of the atoms density field ϕ and the magnetization field $\mathbf{M}$ that are computed by the two schemes SSAV and SAV. From the accuracy plots shown in Fig. 4.1(a), both of the schemes SSAV and SAV present almost perfect second-order accuracy. This implies the stabilizers are not necessary for the low stiffness case. But we still set $S_1 = S_2 = S_3 = 1$ in computations to compare the accuracy rate. We also see that the magnitude of errors generated by the scheme SSAV is relatively larger than that of the scheme SAV since extra splitting errors are introduced by the three extra stabilization terms.

Second, we test the high stiffness case by setting $\gamma = 1, \eta = -100$. We set the stabilization parameters $S_1 = 5, S_2 = S_3 = 100$. In Fig. 4.1(b), the average of L^2 numerical errors of phase-field variable ϕ and magnetization field $\mathbf{M}$ are plotted. We find the scheme SAV loses the accuracy when the time step is larger than $0.1/2^{12}$. Only for smaller time steps of $\delta t \le 0.1/2^{12}$, the scheme SAV exhibits the second-order convergence rate. On the contrary, the scheme SSAV always presents second-order accuracy for all tested time steps which means the stability is controlled well by the stabilization terms.

Finally, we testify whether the stabilized scheme SSAV is unconditionally energy stable by plotting energy evolution curves with different time steps. We still use the previous accuracy example of the high stiffness case. In Fig. 4.2(a), we plot the evolution curves of the total free energy (2.1) that is calculated by the scheme SSAV with ten different time steps from $\delta t = 1$ to $\delta t = \frac{1}{2^9}$ with a factor of $\frac{1}{2}$. All obtained energy curves show monotonic attenuation, which indicates that the scheme SSAV is unconditionally stable. For comparisons, we plot the energy evolution curves computed by the non-stabilized scheme SAV in Fig. 4.2(b). The scheme SAV blows up for all $\delta t > 0.1/2^{16}$ and the energy shows oscillations when $\delta t = 0.1/2^{16}$. The energy curve computed by SAV with

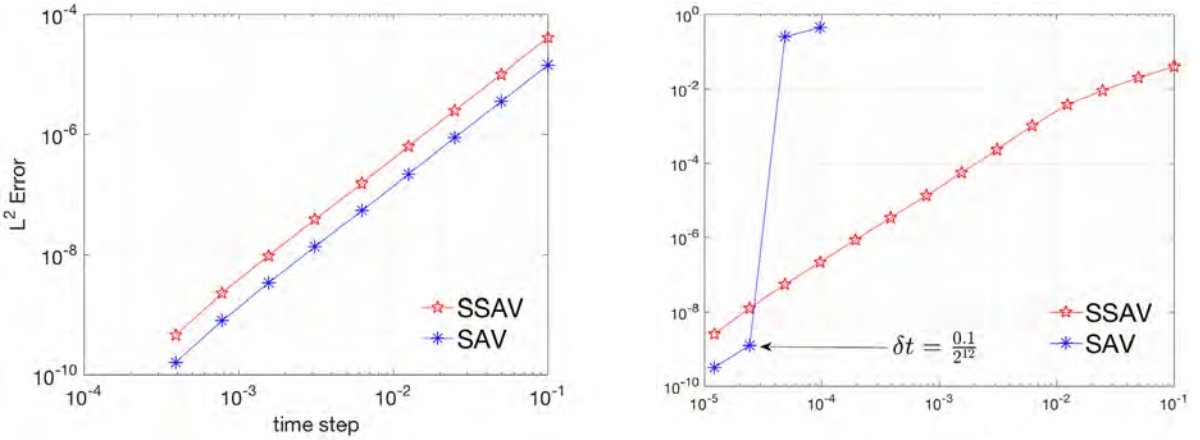

(a) $\gamma = 0.01, \eta = 1.$ (b) $\gamma = 1, \eta = 100.$

Fig. 4.1. The average of the L^2 numerical errors for the atoms density field ϕ and the magnetization field $\mathbf{M}$ with various time steps that are computed using the schemes SSAV and SAV. The two parameters γ, and η are set as (a) $\gamma = 0.01, \eta = 1$ (low stiffness case), and (b) $\gamma = 1, \eta = 100$ (high stiffness case).

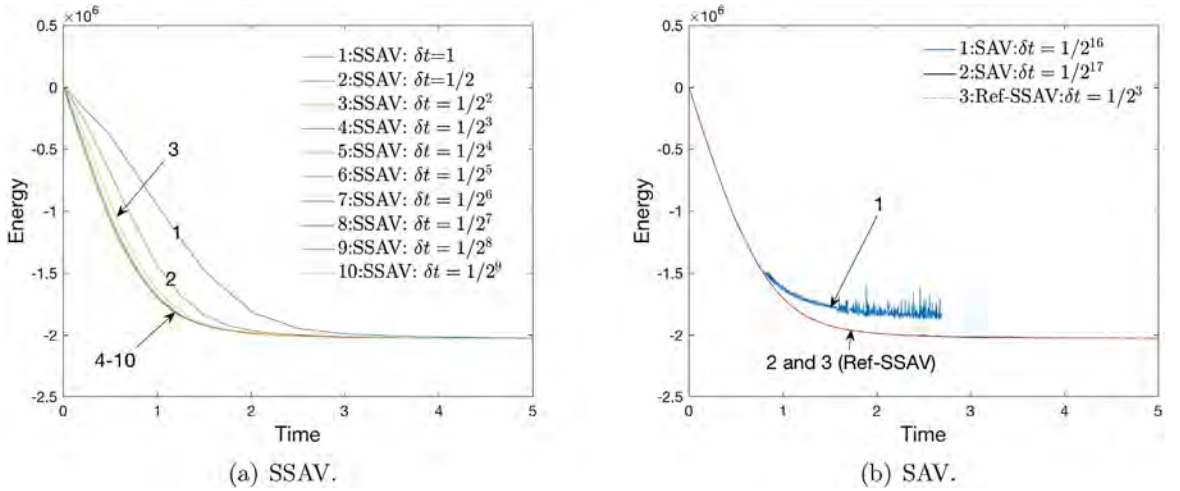

(a) SSAV. (b) SAV.

Fig. 4.2. Time evolution of the total free energy (2.1) computed by the scheme (a) SSAV and (b) SAV with various time step sizes for the high stiffness parameter set $\gamma = 1, \eta = 100$. (Note: we only plot the energy curves computed by SAV with $\delta t = \frac{1}{2^{16}}$ and $\frac{1}{2^{17}}$ in (b). This is because the scheme SAV blows up for $\delta t > \frac{1}{2^{16}}$, thus the associated energy curves are omitted here. For comparisons, the energy curve computed by SSAV with $\delta t = \frac{1}{2^3}$ is used as the reference solution.).

$\delta t = 0.1/2^{17}$ agrees well with that computed by SSAV with $\delta t = 0.1/2^3$, which implies the time step adopted in SSAV can be 2^{14} times larger than that of the scheme SAV to achieve two energy evolution profiles with no visible difference for this particular high stiffness case.

In summary, from the performance of the two schemes SSAV and SAV, we conclude that the stabilized scheme SSAV is stable for all tested time steps and performs very good approximations and second-order accuracy all along.

4.2. Crystal growth

In this subsection, we simulate the growth of tiny crystallites in a supercooled liquid by solving the magnetic-coupled model by implementing the developed scheme SSAV. The initial conditions were set as one or more tiny

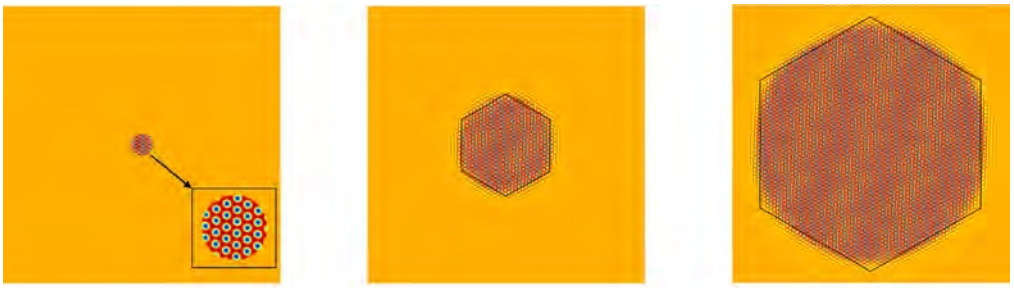

(a) Magnetic-free case at $t = 0$, 200, and 500.

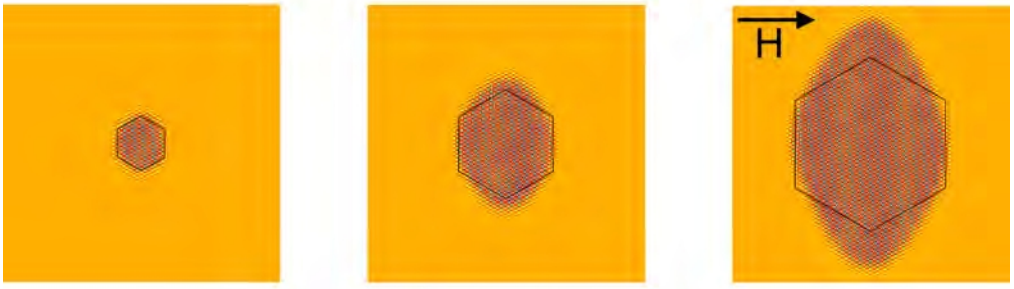

(b) Magnetic-coupled case with $\hat{\mathbf{n}} = (1, 0)$ at $t = 200$, 600, and 1600.

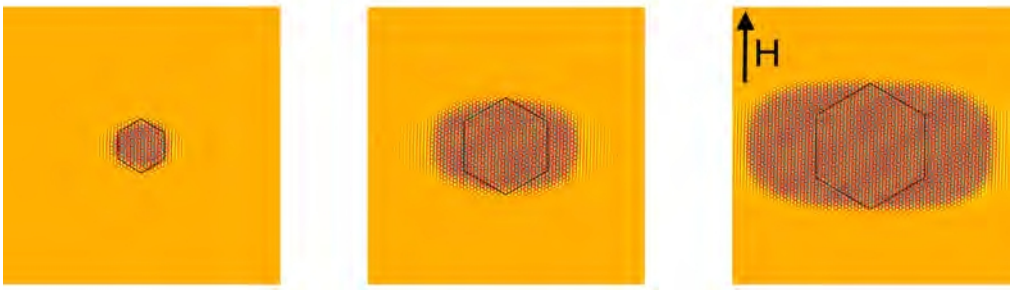

(c) Magnetic-coupled case with $\hat{\mathbf{n}} = (0, 1)$ at $t = 200$, 600, and 1000.

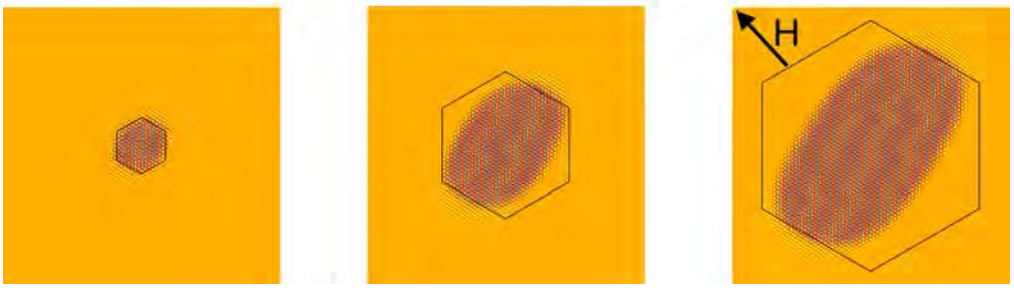

(d) Magnetic-coupled case with $\hat{\mathbf{n}} = (-0.707, 0.707)$ at $t = 200$, 600, and 1000.

Fig. 4.3. The 2D crystal growth example with the initial condition of one small crystallite as a seed that is deposited in the center of the computed domain, where (a) is the magnetic-free case, and (b), (c), (d) are the magnetic-coupled cases with $\hat{\mathbf{n}} = (1, 0)$, $(0, 1)$, and $(-0.707, 0.707)$, respectively. The model parameters are given in (4.3). (Note: in each snapshot, a black hexagonal frame is superimposed to highlight the displacement between the ordered pattern and the regular hexagon).

crystallites with different orientations deposited inside a computational domain. The liquid-crystal interfaces with grain boundaries separating the crystals are formed when the time evolves. The crystal growth for the magnetic-free PFC model is the classical benchmark simulation, see [1,13,16,25,26].

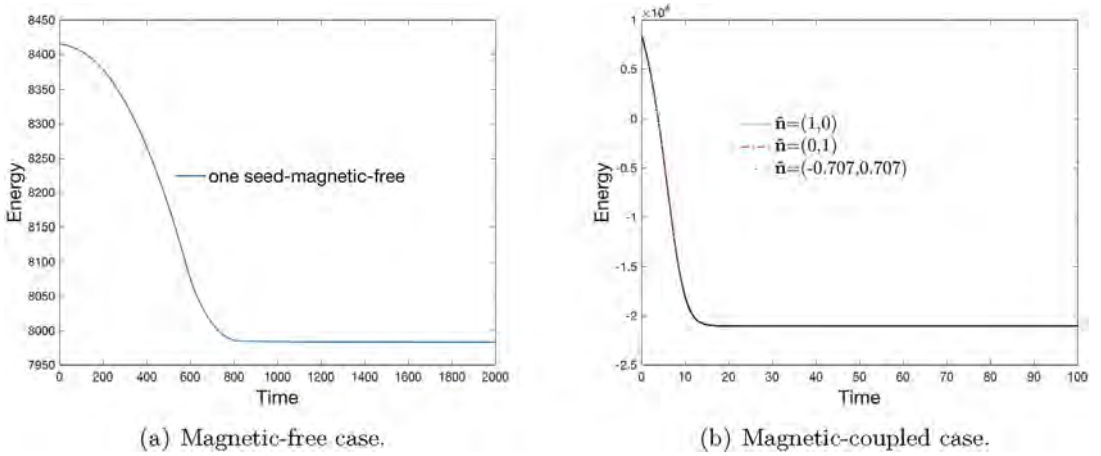

(a) Magnetic-free case. (b) Magnetic-coupled case.

Fig. 4.4. Time evolution of the total free energy (2.1) for the 2D crystal growth example with the initial condition of one seed where (a) is the magnetic-free case, and (b) is the magnetic-coupled case with $\hat{\mathbf{n}} = (1, 0)$, $\hat{\mathbf{n}} = (0, 1)$, and $\hat{\mathbf{n}} = (-0.707, 0.707)$.

We first perform 2D simulations to investigate how a tiny crystallite grows up. The computed domain is set as $[0, L]^2$ with $L = 512$ and we use 513^2 Fourier modes to discretize the space. If not explicitly specified, the model parameters are set as

$$\begin{cases} M_1 = 1,\ B = 1\text{e}7, q_0 = 1, \epsilon = 0.25, \alpha = 1, \beta = 10, M_2 = 0.1, \\ \gamma = 0.1, \eta = -0.4, \theta_1 = \theta_2 = 1\text{e} - 9, S_1 = S_2 = S_3 = 2. \end{cases} \tag{4.3}$$

To obtain the initial configuration of a regular tiny crystallite as a seed, we first implement the scheme SSAV to solve the magnetic-free model for a sufficiently long time and cut a patch from the center region. The detailed process to get the initial condition of $\phi^0(x, y)$ is described as follows.

- First, we define a function $\Phi(x, y)$ to be a constant value and then modify it by superimposing some trigonometric oscillations in a small circular patch, as follows:

$$\Phi(x, y) = \begin{cases} \bar{\phi} + q\Big(\cos(\frac{p}{\sqrt{3}} y_l)\cos(p x_l) - 0.5\cos(\frac{2p}{\sqrt{3}} y_l)\Big), & \text{if } (x, y) \in D, \\ \bar{\phi}, & \text{else}, \end{cases} \tag{4.4}$$

  where D represents a small circular patch in the center of the domain that is given as

$$D = \{(x, y) : (x - L/2)^2 + (y - L/2)^2 \le r^2\}, \tag{4.5}$$

  and $(r, \bar{\phi}, p, q) = (10, 0.285, 0.66, 0.446)$. (x_l, y_l) defines a local system of Cartesian coordinates that is oriented with the crystallite lattice which is formulated by using an affine transformation of the global Cartesian coordinates (x, y), i.e.,

$$(x_l, y_l) = (x\sin(\theta) + y\cos(\theta), -x\cos(\theta) + y\sin(\theta)), \tag{4.6}$$

  where $\theta = 0$ (note one can set any arbitrarily chosen values for θ to obtain various patterns with different orientations). By taking $\Phi(x, y)$ as the initial condition, we implement the scheme SSAV for the sufficient long time ($t = 3000$) to arrive at an intermediate profile of $\hat{\Phi}(x, y)$.
- Then, we cut the small patch D from the intermediate profiles $\hat{\Phi}(x, y)$ and use it as the initial condition of $\phi^0(x, y)$, i.e.

$$\phi^0(x, y) = \begin{cases} \hat{\Phi}(x, y), & \text{if } (x, y) \in D, \\ \bar{\phi}, & \text{else}. \end{cases} \tag{4.7}$$

We obtain the initial condition $\phi^0(x, y)$ of a small crystallite from the above process. The profile is shown in the first subfigure in Fig. 4.3(a) where we superimpose a small inset figure to show the detailed contour of the initial

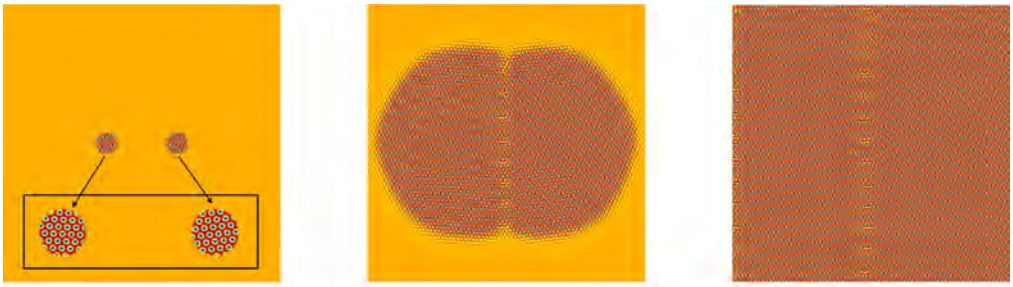

(a) Magnetic-free case at $t = 0$, 400, 800.

(b) Magnetic-coupled case with $\hat{\mathbf{n}} = (1, 0)$ at $t = 200$, 400, 2000.

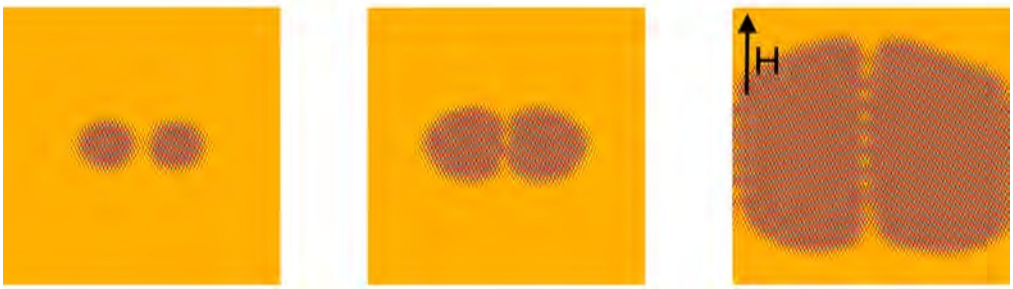

(c) Magnetic-coupled case with $\hat{\mathbf{n}} = (0, 1)$ at $t = 200$, 400, 2000.

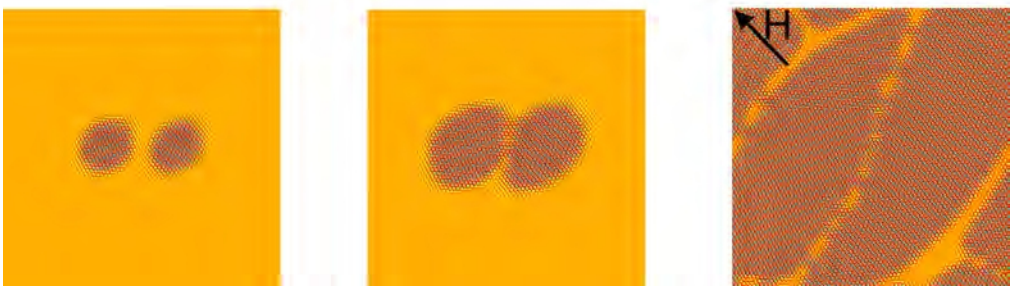

(d) Magnetic-coupled case with $\hat{\mathbf{n}} = (-0.707, 0.707)$ at $t = 200$, 400, and 2000.

Fig. 4.5. The 2D crystal growth example with the initial condition of two small twin seeds that are deposited symmetrically in the computed domain, where (a) is the magnetic-free case, and (b), (c), (d) are the magnetic-coupled cases with $\hat{\mathbf{n}} = (1, 0)$, $(0, 1)$, and $(-0.707, 0.707)$, respectively. The model parameters are given in (4.3).

profile. We first perform the simulation for the magnetic-free case by setting $\mathbf{H} = 0, \gamma = \eta = \theta_2 = 0$ and plot several snapshots of ϕ in Fig. 4.3(a). We observe that the small crystallite grows up and the pattern is ordered in the hexagonal phase. At each snapshot, a black hexagonal frame is superimposed outside the crystals to highlight the good agreement between the formed pattern of atoms and the standard hexagon.

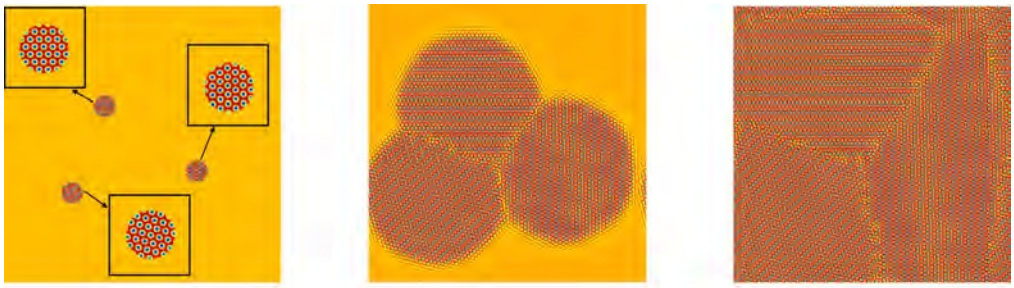

(a) Magnetic-free case at $t = 0$, 300, 700.

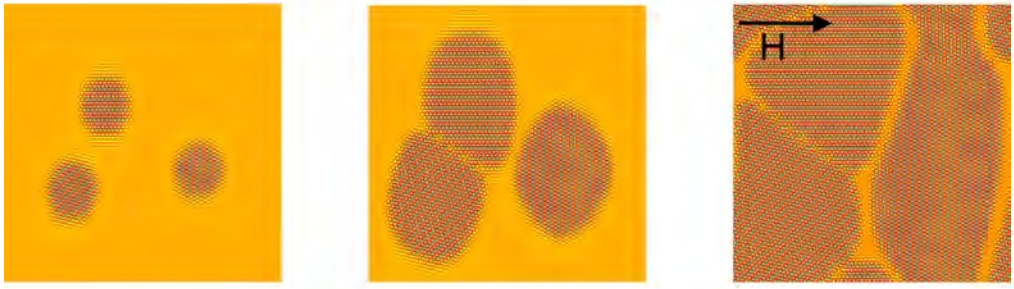

(b) Magnetic-coupled case with $\hat{\mathbf{n}} = (1, 0)$ at $t = 200$, 600, 2000.

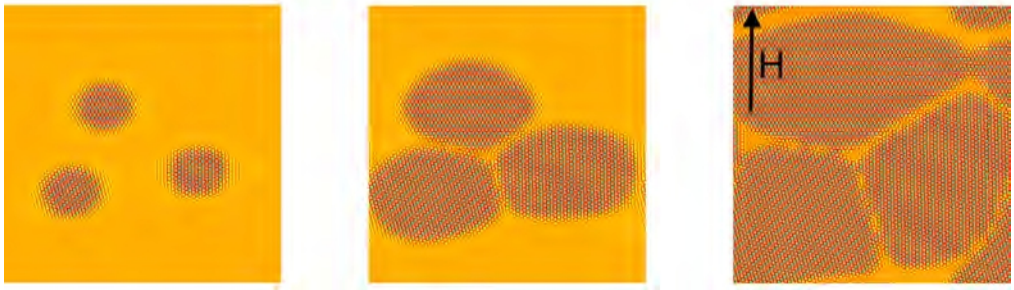

(c) Magnetic-coupled case with $\hat{\mathbf{n}} = (0, 1)$ at $t = 200$, 600, 2000.

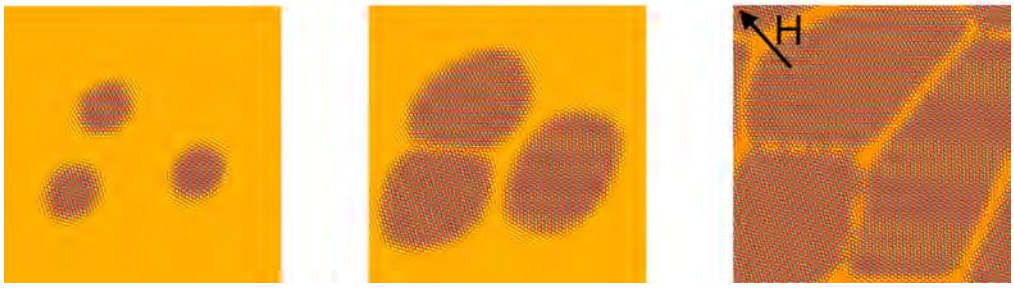

(d) Magnetic-coupled case with $\hat{\mathbf{n}} = (-0.707, 0.707)$ at $t = 200$, 600, 2000.

Fig. 4.6. The 2D crystal growth example with the initial condition of three small arbitrarily deposited seeds, where (a) is the magnetic-free case, and (b), (c), (d) are the magnetic-coupled cases with $\hat{\mathbf{n}} = (1, 0)$, $(0, 1)$, and $(-0.707, 0.707)$, respectively. The model parameters are given in (4.3).

We further investigate the crystal growth for the magnetic-coupled case. We still use the same initial condition of one seed and set the initial condition of the magnetization field as $\mathbf{M}^0 = 0$. The applied external magnetic field is set as $\mathbf{H} = 0.25\hat{\mathbf{n}}$ where $\hat{\mathbf{n}}$ represents the unit direction vector. In Fig. 4.3(b), (c), and (d), we present the profiles of the phase-field variable ϕ by setting $\hat{\mathbf{n}} = (1, 0)$, $(0, 1)$, and $(-0.707, 0.707)$, respectively. In each snapshot, the

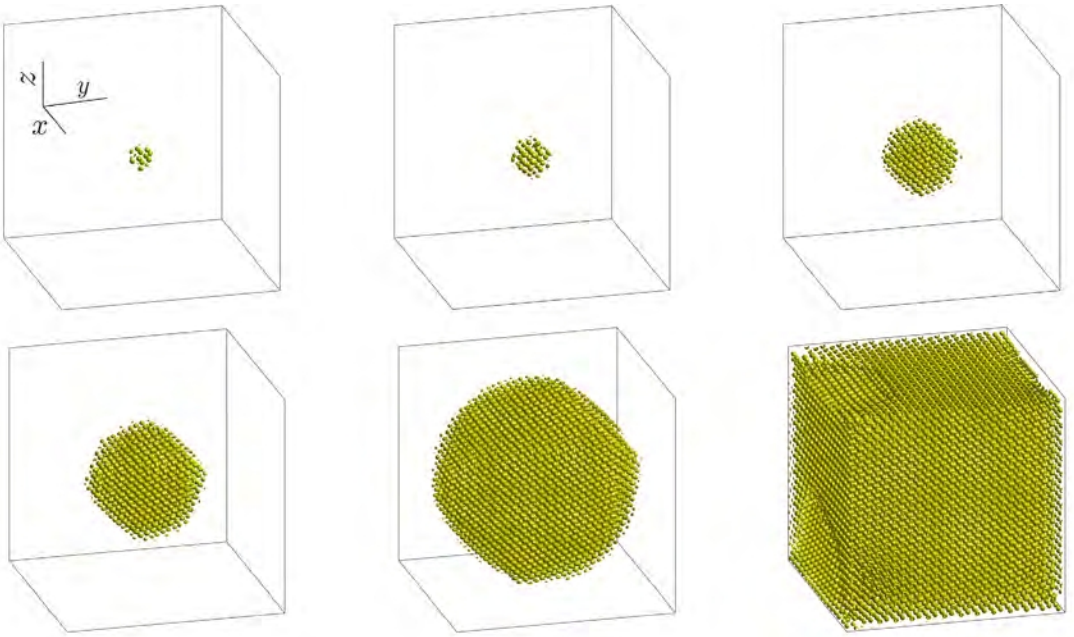

(a) Snapshots of the isosurfaces of $\{\phi = -0.1\}$ at $t = 0, 100, 200, 300, 500$, and 2000.

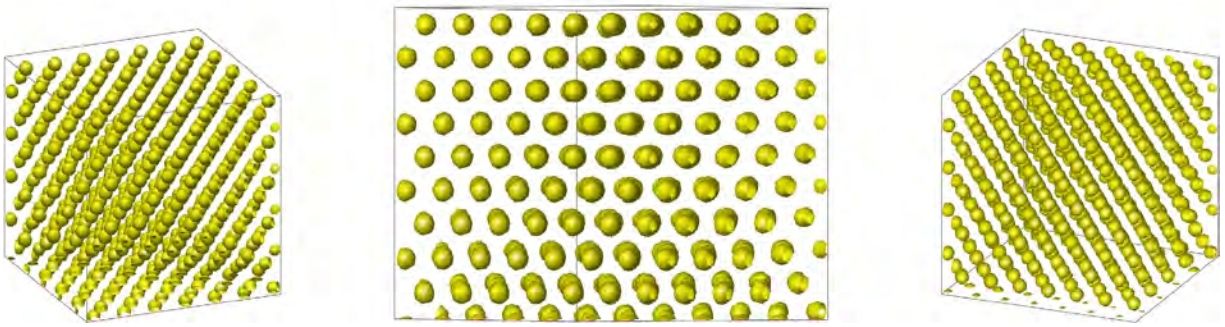

(b) A close-up view for a small cube $[0, 60]^3$ with three different view angles.

Fig. 4.7. The 3D crystal growth example for the magnetic-free case with the initial condition of one seed deposited in the center, where (a) is the snapshots of the isosurfaces $\{\phi = -0.1\}$ that are taken at $t = 0$, 100, 200, 300, 500, and 2000, and (b) is the close-up view of the isosurfaces for a small cube $[0, 60]^3$ with three different view angles. The model parameters are from (4.3).

black hexagonal frame is also superimposed to highlight the displacement of the atomic locations, where we see that the formed regiment of atoms deviates from the hexagonal frame largely. Meanwhile, the main direction of atoms growth is always perpendicular to the applied magnetic field $\mathbf{H}$. These results are qualitatively consistent with the simulations presented in [12].We plot the time evolution curves of the total free energy in Fig. 4.4.

Continuously, we set the initial conditions to be a twin crystallite seed where the initial conditions are obtained by repeating the above procedure and changing the small patch D to be two small circular patches, shown in the first subfigure in Fig. 4.5(a). When the magnetic field is free, snapshots of dynamical morphology are shown in Fig. 4.5(a) where a long dislocation line is formed vertically due to the different alignment of the twin crystals. In Fig. 4.5(b), (c), and (d), we show the growth process by applying the external magnetic field $\mathbf{H} = 0.25\hat{\mathbf{n}}$ with $\hat{\mathbf{n}} = (1, 0), (0, 1)$, and $(-0.707, 0.707)$, respectively. Similar to the one-seed case, the main direction of atoms growth is always perpendicular to the applied magnetic field $\mathbf{H}$.

The dynamical process of crystal growth of three arbitrarily deposited seeds for the magnetic-free case is shown in Fig. 4.6(a), where more dislocation lines and defects are formed due to the orientation discrepancy while the

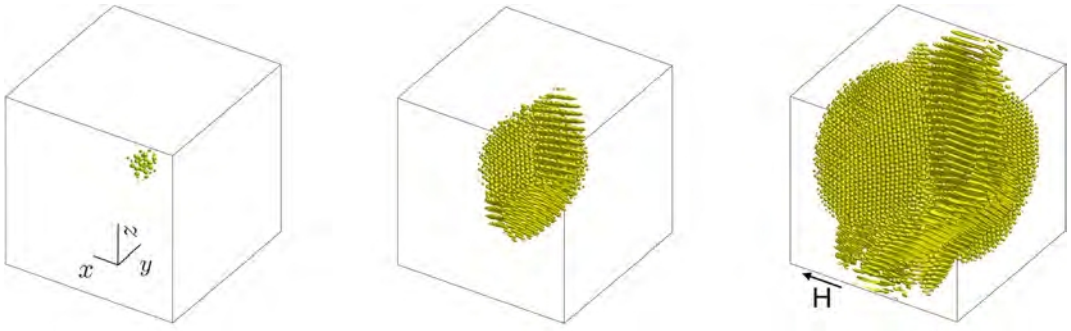

(a) $\hat{\mathbf{n}} = (1, 0, 0)$ and snapshots are taken at $t = 100$, 500, and 1000.

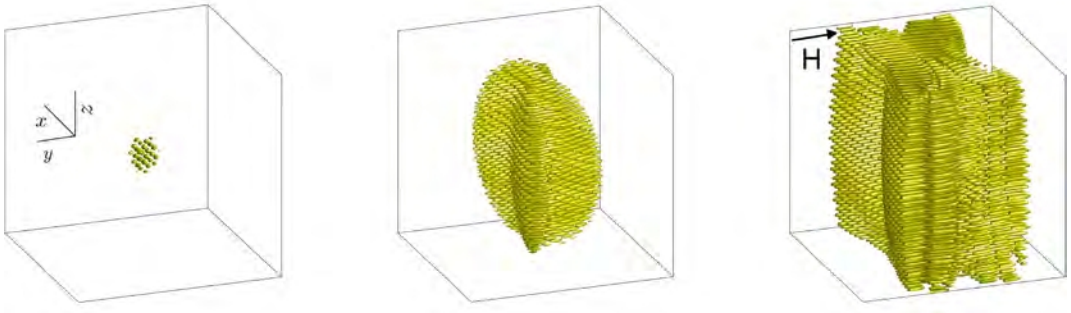

(b) $\hat{\mathbf{n}} = (0, 1, 0)$ and snapshots are taken at $t = 100$, 500, and 1000.

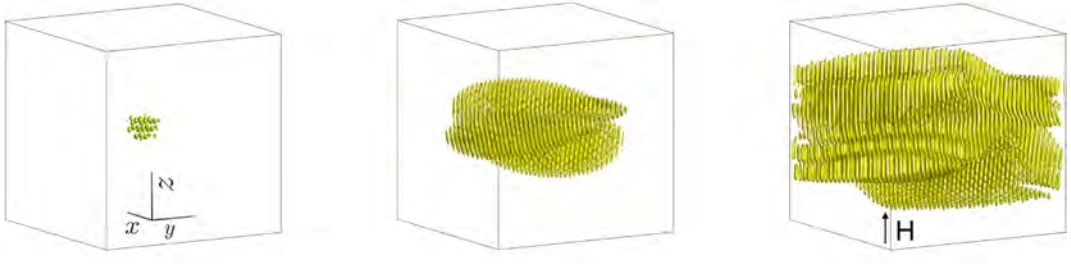

(c) $\hat{\mathbf{n}} = (0, 0, 1)$ and snapshots are taken at $t = 100$, 500, and 1000.

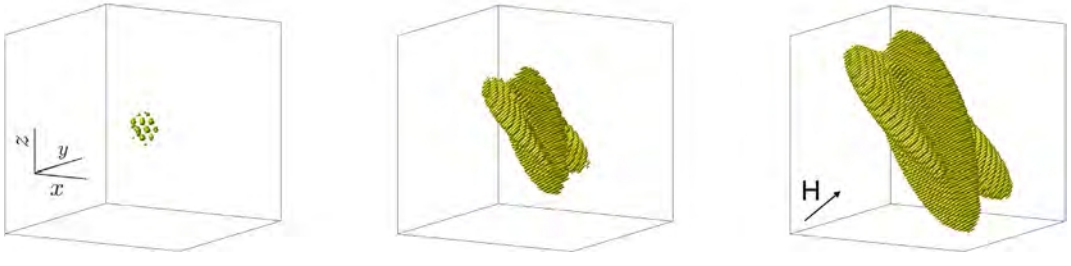

(d) $\hat{\mathbf{n}} = (-0.577, -0.577, 0.577)$ and snapshots are taken at $t = 100$, 400, and 600.

Fig. 4.8. The 3D crystal growth example for the magnetic-coupled case with the initial condition of one seed deposited in the center, where (a) $\hat{\mathbf{n}} = (1, 0, 0)$, (b) $\hat{\mathbf{n}} = (0, 1, 0)$, (c) $\hat{\mathbf{n}} = (0, 0, 1)$, and (d) $\hat{\mathbf{n}} = (-0.577, -0.577, 0.577)$. The model parameters are all from (4.3).

crystallites grow up. The dynamical crystal growth process under the magnetic field is presented in Fig. 4.6(b), (c), and (d).

We finally simulate the growth process for the one-seed case in 3D where the computational domain is set as $[0, L]^3$ with $L = 200$ and space is discretized by using 201^3 Fourier modes. The model parameters are still from

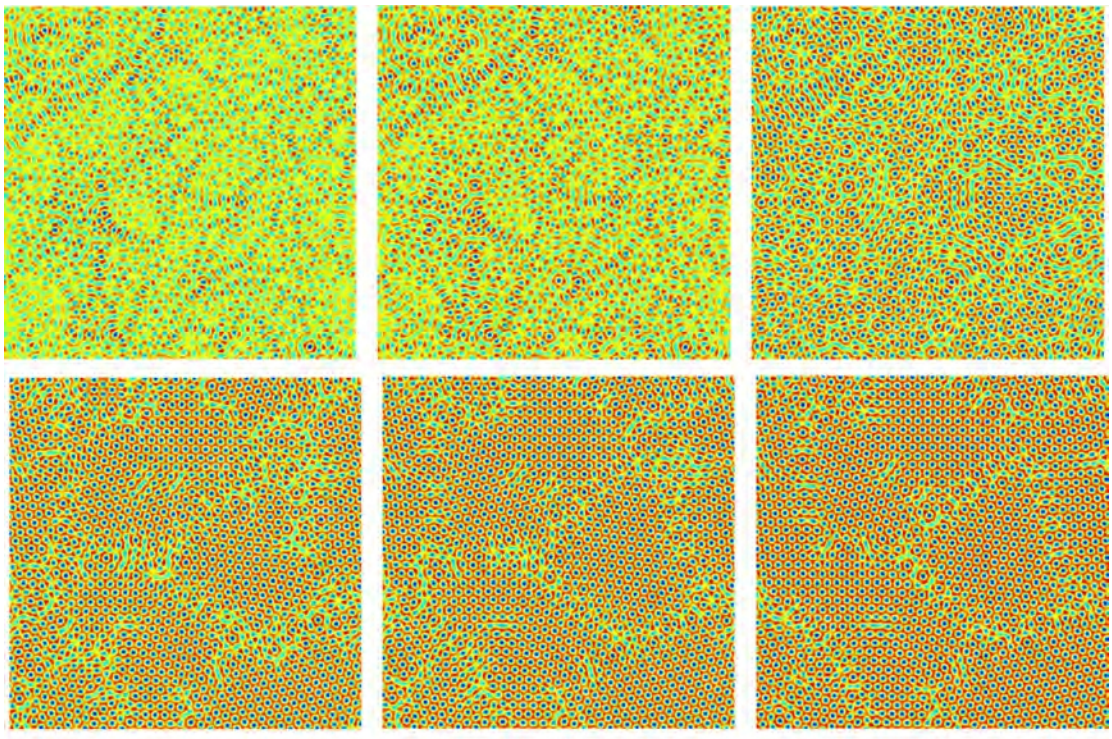

(a) Magnetic-free case where snapshots are taken at $t = 80$, 100, 200, 400, 600, and 1000.

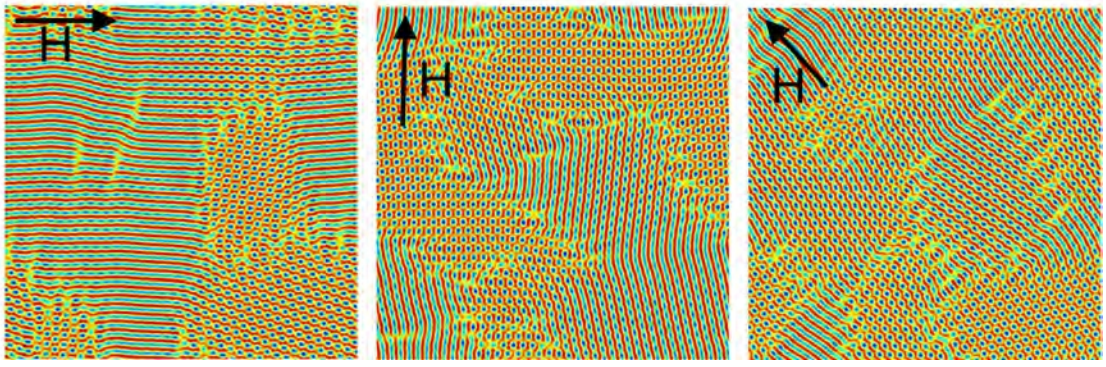

(b) $\hat{\mathbf{n}} = (1, 0)$. (c) $\hat{\mathbf{n}} = (0, 1)$. (d) $\hat{\mathbf{n}} = (-0.707, 0.707)$.

Fig. 4.9. (a) The 2D pattern formation of crystal lattice for the phase separation example for the magnetic-free case at various times. The equilibrium solutions are obtained for the magnetic-coupled case where (b) $\hat{\mathbf{n}} = (1, 0)$, (c) $\hat{\mathbf{n}} = (0, 1)$, and (d) $\hat{\mathbf{n}} = (-0.707, 0.707)$.

(4.3). The initial condition, shown in the first subfigure of Fig. 4.7(a), is obtained by performing a similar process as the 2D example. The dynamical growth process for the magnetic-free case is shown in Fig. 4.7(a), where the isosurfaces of $\{\phi = -0.1\}$ are plotted. We see that the tiny crystallite finally grows up to the whole computed domain and the equilibrium solution presents the BCC pattern. To get a more accurate view, we enlarge a local region $[0, 60]^3$ in Fig. 4.7(b) with three different view angles which clearly show the BCC structures in 3D. In Fig. 4.8, we simulate the magnetic-coupled cases by applying the external magnetic field $\mathbf{H} = 0.25\hat{\mathbf{n}}$ with four directions of $\hat{\mathbf{n}} = (1, 0, 0)$, $(0, 1, 0)$, $(0, 0, 1)$, and $(-0.577, -0.577, 0.577)$, respectively. The process of crystal growth presents anisotropy and the main growth direction of atoms is always perpendicular to the applied magnetic field $\mathbf{H}$ which is consistent with the 2D simulations.

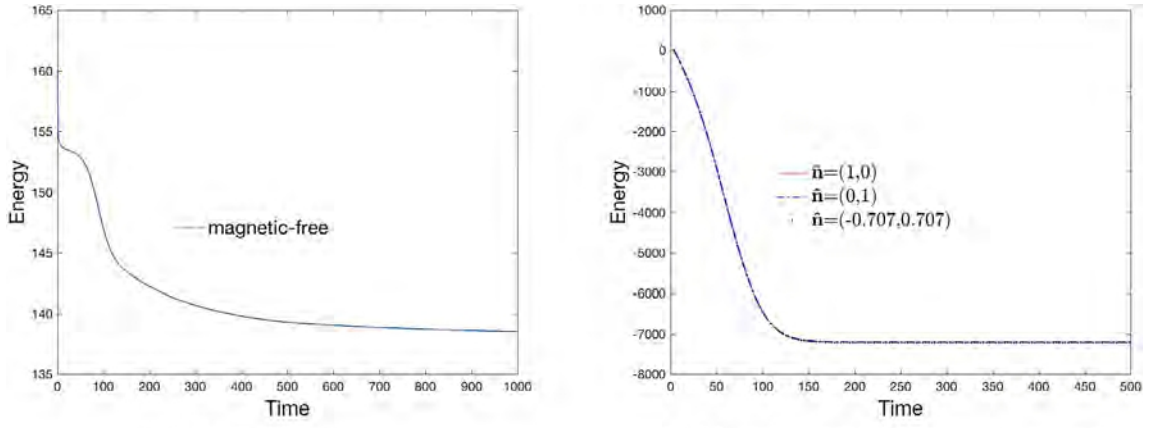

(a) Magnetic-free case. (b) Magnetic-coupled case with various $\hat{\mathbf{n}}$.

Fig. 4.10. Time evolution of the total free energy (2.1) for the 2D phase separation example where (a) is the magnetic-free case, and (b) is the magnetic-coupled case with $\hat{\mathbf{n}} = (1, 0)$, $(0, 1)$, and $(-0.707, 0.707)$.

4.3. Phase transitions

In this subsection, we simulate the phase transition behaviors of the FMPFC model by using the developed scheme SSAV. The initial conditions are set as a homogeneous mixture with random perturbations for $\phi^0(x, y)$. Due to the spontaneous growth of the concentration fluctuations, the homogeneous state of the system will evolve to the different phases.

We implement 2D simulations and set the computational domain as $\Omega = [0, 256]^2$ which is then discretized using 257^2 Fourier modes. The initial conditions read as

$$\phi^0(x, y) = \bar{\phi} + 0.001\text{rand}(x, y), \tag{4.8}$$

where $\bar{\phi}$ is the initial average, rand(x, y) is the random number in the range of $[-1, 1]$. If not explicitly specified, we set the model parameters as

$$\begin{cases} M_1 = 1,\ B = 1\text{e}7, q_0 = 1, \epsilon = 0.05, \alpha = 1, \beta = 10, M_2 = 0.01, \\ \gamma = 0.01, \eta = -0.1, \theta_1 = \theta_2 = 1\text{e} - 9, S_1 = S_2 = S_3 = 2. \end{cases} \tag{4.9}$$

We set $\bar{\phi} = 0.07$ and perform a simulation for the magnetic-free case by setting $\mathbf{H} = 0$, $\gamma = \eta = 0$. Snapshots of the phase-field variable ϕ at various times until that the equilibrium states are shown in Fig. 4.9(a) for the magnetic-free case, where we observe that the atoms are generated from the homogeneous state and many dislocations are presented.

To see the effects from the magnetic field, we take the equilibrium solution of the magnetic-free case as the initial condition for the magnetic-coupled simulations. By applying the external magnetic field $\mathbf{H} = 0.25\hat{\mathbf{n}}$ with three different directions of $\hat{\mathbf{n}} = (1, 0)$, $(0, 1)$, and $(-0.707, 0.707)$, we plot the obtained equilibrium state solutions in Fig. 4.9(b)–(d). With the applied magnetic field, we find that the final equilibrium solutions of the density of the atoms ϕ present the mixed-phase between the strips and BCC phase, and the orientation of the stripe phase is always parallel to the direction $\hat{\mathbf{n}}$. The time evolutions of the total free energy for all these simulations are presented in Fig. 4.10, that shows the monotonic decays with time.

5. Concluding remarks

We consider numerical approximations for the magnetic-coupled phase-field-crystal model in this paper. The model consists of two strongly coupled nonlinear equations. To solve the model, we develop an efficient scheme by combining the recently developed SAV approach with several added stabilization terms. For the high stiffness case, the stabilization terms are critical to improve the stability particularly when large time steps are used. The

scheme is easy to implement practically and also provably unconditionally energy stable. In simulating numerous benchmark numerical examples including the accuracy/stability tests, the crystal growth and phase transitions in 2D and 3D, the stability and the accuracy of the developed scheme are demonstrated numerically. To the best of the author's knowledge, this is the first such a scheme that is second-order accurate in time, linear, decoupled, and unconditionally energy stable for the magnetic-coupled PFC model.

Declaration of competing interest

The authors declare that they have no known competing financial interests or personal relationships that could have appeared to influence the work reported in this paper.

Acknowledgments

The work of Jun Zhang is supported by the National Natural Science Foundation of China (No. 11901132). X. Yang was partially supported by National Science Foundation with grant numbers DMS (1720212, 1818783, and 2012490).

References

[1] K.R. Elder, M. Katakowski, M. Haataja, M. Grant, Modeling elasticity in crystal growth, Phys. Rev. Lett. 88 (24) (2002) 245701.
[2] K.R. Elder, M. Grant, Modeling elastic and plastic deformations in nonequilibrium processing using phase field crystals, Phys. Rev. E. 70 (2004) 051605.
[3] P.Y. Chan, N. Goldenfeld, J. Dantzig, Molecular dynamics on diffusive time scales from the phase-field-crystal equation, Phys. Rev. E. 79 (2009) 035701R.
[4] P. Stefanovic, M. Haataja, N. Provatas, Phase-field crystals with elastic interactions, Phys. Rev. Lett. 96 (2006) 225504.
[5] P. Stefanovic, M. Haataja, N. Provatas, Phase field crystal study of deformation and plasticity in nanocrystalline materials, Phys. Rev. E 80 (2009) 046107.
[6] A. Toyotama, T. Okuzono, J. Yamanaka, Spontaneous formation of eutectic crystal structures in binary and ternary charged colloids due to depletion attraction, Sci. Rep. 6 (2016) 23292.
[7] P.Y. Chan, (Ph.D. thesis), University of Illinois at Urbana Champaign, 79, 2007.
[8] J. Berry, M. Grant, Modeling multiple time scales during glass formation with phase-field crystals, Phys. Rev. Lett. 106 (2011) 175702.
[9] G. Tegze, G. Bansel, G.I. Tóth, T. Pusztai, Z. Fan, L. Gránásy, Advanced operator splitting-based semi-implicit spectral method to solve the binary phase-field crystal equations with variable coefficients, J. Comput. Phys. 228 (5) (2009) 1612–1623.
[10] N. Faghihi, S. Mkhonta, K. Elder, M. Grant, Magnetic islands modelled by a phase-field-crystal approach, Eur. Phys. J. B 91 (2018) 55.
[11] N. Faghihi, N. Provatas, K.R. Elder, M. Grant, M. Karttunen, Phase-field-crystal model for magnetocrystalline interactions in isotropic ferromagnetic solids, Phys. Rev. E. 88 (2013) 032407.
[12] M. Seymour, F. Sanches, K. Elder, N. Provatas, Phase-field crystal approach for modeling the role of microstructure in multiferroic composite materials, Phys. Rev. E. 92 (2015) 184109.
[13] C. Wang, S.M. Wise, An energy stable and convergent finite-difference scheme for the modified phase field crystal equation, SIAM J. Numer. Anal. 49 (2011) 945–969.
[14] S.M. Wise, C. Wang, J.S. Lowengrub, An energy-stable and convergent finite-difference scheme for the phase field crystal equation, SIAM J. Numer. Anal. 47 (3) (2009) 2269–2288.
[15] J. Zhang, X. Yang, On efficient numerical schemes for a two-mode phase field crystal model with face-centered-cubic (FCC) ordering structure, Appl. Numer. Math. 146 (2019) 13–37.
[16] H. Gomez, X. Nogueira, An unconditionally energy-stable method for the phase field crystal equation, Comput. Methods Appl. Mech. Engrg. 249–252 (2012) 52–61.
[17] X. Yang, D. Han, Linearly first- and second-order, unconditionally energy stable schemes for the phase field crystal equation, J. Comput. Phys. 330 (2017) 1116–1134.
[18] J. Shen, J. Xue, J. Yang, The scalar auxiliary variable (SAV) approach for gradient flows, J. Comput. Phys. 353 (2018) 407–416.
[19] Q. Cheng, J. Shen, Multiple scalar auxiliary variable (MSAV) approach and its application to the phase-field vesicle membrane model, SIAM. J. Sci. Comput. 40 (2018) A3982–A4006.
[20] C. Chen, X. Yang, Efficient numerical scheme for a dendritic solidification phase field model with melt convection, J. Comput. Phys. 388 (2019) 41–62.
[21] X. Yang, Linear, first and second order and unconditionally energy stable numerical schemes for the phase field model of homopolymer blends, J. Comput. Phys. 327 (2016) 294–316.
[22] C. Chen, X. Yang, Fast, provably unconditionally energy stable, and second-order accurate algorithms for the anisotropic Cahn–Hilliard model, Comput. Methods Appl. Mech. Engrg. 351 (2019) 35–59.
[23] J. Zhang, C. Chen, X. Yang, A novel decoupled and stable scheme for an anisotropic phase-field dendritic crystal growth model, Appl. Math. Lett. 95 (2019) 122–129.
[24] P.M. Chaikin, T.C. Lubensky, Principles of Condensed Matter Physics, Cambridge University Press, Cambridge, 2000.
[25] Z. Hu, S.M. Wise, C. Wang, J.S. Lowengrub, Stable and efficient finite difference nonlinear-multigrid schemes for the phase field crystal equation, J. Comput. Phys. 228 (2009) 5323–5339.
[26] K. Wu, A. Adland, A. Karma, Phase-field-crystal model for fcc ordering, Phys. Rev. E 81 (2010) 061601.